This article has been accepted for publication in IEEE Sensors Journal. This is the author's version which has not been fully edited and content may change prior to final publication. Citation information: DOI 10.1109/JSEN.2025.3574232

Validation of a MEMS-Based Pressure Sensor System for Atrial Fibrillation Detection from Wrist and Finger

Yangyang Zhao[1], Olli Lahdenoja[1], Ismail Elnaggar[1], Tuija Vasankari[2], Samuli Jaakkola[2], Tuomas Kiviniemi[2], Juhani Airaksinen[2], Matti Kaisti[1], and Tero Koivisto[1]

***Abstract*—To address the unmet need for a low-cost, low-power wearable solution for continuous cardiovascular health monitoring, we developed and validated an Atrial Fibrillation (AF) detection algorithm using clinical data collected with a microelectromechanical system (MEMS)-based pressure sensor. This sensor system, consisting of a circuit board, capacitive digitizer, and three MEMS elements, was specifically designed for early detection of AF—a common cardiac arrhythmia that requires frequent screening. The proposed algorithm extracts seven AF-related features, derived from autocorrelation analysis, Inter-Beat Interval (IBI) measurements, and differential IBI (dIBI) analysis, including a novel Mean Distance of Points in the Poincaré Plot (MDPP) feature. Clinical validation was conducted using data from 53 participants across three datasets: 13 healthy volunteers (wrist), 20 post-cardiac surgery sinus rhythm patients (wrist), and 20 AF patients (wrist and finger). Leave-one-out cross-validation showed that logistic regression achieved an AUROC of 93.0% using the full feature set. Performance remained stable across segment lengths ranging from 10 to 120 seconds, supporting the algorithm's suitability for continuous monitoring. Consistent performance across seven different classifiers (average AUROC 92.1%) further demonstrated the clinical applicability and generalizability of the approach for wearable-based AF screening. To assess robustness against motion artifacts, we introduced five types of synthetic noise, with the algorithm maintaining strong AF detection performance under these conditions. Finally, a systematic evaluation of sensor waveform shape and signal strength across sinus rhythm and AF, at both wrist and finger sites demonstrates the potential of the sensor system for wearable AF screening.**

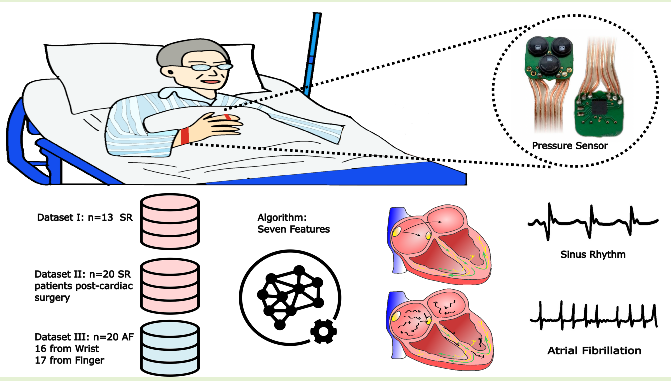

***Index Terms*—Atrial Fibrillation (AF), Machine learning, Microelectromechanical sensor (MEMS), Pressure, Sensor, Wearables**

I. INTRODUCTION

ATRIAL fibrillation (AF) is a prevalent cardiac arrhythmia that requires frequent screening and considerably contributes to stroke and heart disease-related mortality [1]. AF is estimated to affect roughly 3% of the adult population worldwide, or around 34 million individuals [2]. Despite its high prevalence, AF often remains undetected and underdiagnosed.

Smartwatches can detect AF using photoplethysmography (PPG) signals or electrocardiography (ECG) signals, such as the Apple watch or the HUAWEI watch. The PPG-based watch's advantage is its non-invasive nature and ability for continuous monitoring [3] [4] [5]. However, the optical nature of PPG technology inherently limits power consumption reduction. PPG measurement systems often require frequent recharging, which limits the time for continuous monitoring. Meanwhile, the demand for affordable, non-invasive wearable devices for sustained monitoring of AF and other cardiovascular diseases is on the rise [6] [7].

Opportunely, wearable pressure sensors, with their excellent wear resistance, stability, lightweight nature, and low cost, emerge as an ideal alternative. These include piezoresistive sensors [8] [9], capacitive sensors [10] [11], optical pressure sensors [12] [13], piezoelectric pressure sensors [14] [15], triboelectric pressure sensors [16] [17] and magnetoelastic pressure sensors [18].

The principle of using a pressure sensor to detect blood pressure waveforms is based on measuring pressure changes in the artery as blood moves through the vascular system. The pressure sensor records these changes, forming a waveform that can be divided into systolic and diastolic phases: the

This study was funded by Business Finland's project (543/31/2015).

[1] Y. Zhao, O. Lahdenoja, I. Elnaggar, M. Kaisti, and T. Koivisto are with the Department of Computing, Faculty of Technology, University of Turku, Turku 20520, Finland (e-mail: yangyang.zhao@utu.fi; olanla@utu.fi; ismail.m.elnaggar@utu.fi; mkaist@utu.fi; tejuko@utu.fi).

[2] T. Vasankari, S. Jaakkola, T. Kiviniemi, and J. Airaksinen are with the Heart Center, Turku University Hospital, Turku 20521, Finland (e-mail: tuija.vasankari@tyks.fi; samuli.jaakkola@tyks.fi; tuomas.kiviniemi@tyks.fi; juhani.airaksinen@tyks.fi).

expansion of the arterial system caused by blood inflow leads to a rising systolic wave, which peaks during systole, followed by a notch and the diastolic phase where the waveform gradually decays. These pressure changes reflect blood volume variations and provide indirect information about cardiac activity. However, the waveform is influenced by factors such as vascular compliance, arterial stiffness, pulse wave propagation, and measurement location [19] [20] [21]. For AF characterized by irregular heartbeats these irregularities may be less distinct in peripheral pressure signals due to physiological transformations affecting waveform morphology and beat-to-beat variability [22] [23]. Given these characteristics, the waveforms from pressure sensor-based devices are similar to PPG signals, suggesting that they may serve as an effective alternative or complementary tool for cardiovascular monitoring.

In this study, we comprehensively evaluate a MEMS-based capacitive pressure sensor for continuous monitoring and present a novel AF detection approach, highlighting the following key contributions: (1) We conduct a systematic feature-level evaluation, covering AF-related features, noise robustness against five types of synthetic noise, and morphology-based analysis comparing wrist and finger placements. (2) We extract a set of AF-related features that capture beat-to-beat irregularities, focusing on an autocorrelation-based feature (Autocorrelation Area, AUA) and a new Poincaré-plot-based feature (Mean Distance of Points in the Poincaré Plot, MDPP). (3) We evaluate the impact of signal segment length on AF detection performance across durations ranging from 10 to 120 seconds. (4) We compare the performance of seven machine learning models to provide insights into the optimal model choice for this type of sensor data. (5) We base all analyses on real-world clinical data collected from both the wrist and finger.

This study is organized as follows. Section II provides an overview of sensing systems and human studies. Section III covers signal processing, segmentation, peak detection methods, and feature extraction, in which seven features are extracted for AF detection and three for waveform and signal strength analysis. This section also describes the machine learning models used in the study. In Section IV, we present the results of three experiments, focusing on the performance of the proposed approach across three datasets. Finally, Sections V and VI provide the discussion and conclusions, respectively.

II. METHOD AND MATERIALS

A. Sensing system

The MEMS pressure sensing system comprises a flexible hemispherical silicone gel and a plastic substrate with four embedded contact plates. The circuit board is equipped with an array of three identical MEMS elements, which are responsible for collecting and processing signals. The capacitive digital converter converts analog signals into digital signals for further processing. The sensing system is shown in **Fig. 1 (a), (b)**. These components are assembled on an elastic Velcro band. The sensor system is designed to be flexible and non-invasive.

A MEMS pressure sensor element (SCB10H), capable of measuring absolute pressure from 0-120 kPa was used. It comprises two silicon wafers with dimensions of 1.2 mm × 1.2 mm × 27 μm bonded together by anodes and a glass wafer. One of the silicon wafers acts as a diaphragm, bending in response to external pressure and generating a force proportional to the bending of the diaphragm and the capacitance between the electrodes [24]. The capacitance between the electrodes is proportional to the external pressure. This is illustrated in **Fig. 1 (c)** .

The glass insulator in the SCB10H results in high isolation resistance, which allows for low leakage currents and stray capacitance. This results in high-pressure measurement accuracy and a dynamic change in capacitance value in the measurement range of 30% to 50% of the total capacitance. Furthermore, the SCB10H offers the advantage of ultra-low current consumption and excellent resistance to overvoltage and shock.

A 5 mm diameter hemispherical silicone gel is used to cover the pressure transducer. The pressure transducer is connected to the substrate through gold wires. The substrate features four copper contact plates of equal size at its base, which are used for characterizing the pressure transducer and verifying its accuracy through measurements.

A printed circuit board was used to mount the three pressure sensor elements. An Acam PCap04 capacitance-to-digital converter (CDC) is used to measure the capacitance of the three sensors. The element itself is passive, the leakage current is shallow, and most of the power consumed is due to the high-frequency charging and discharging of the capacitive element [25] [26], which is the main reason for its low power consumption characteristics. To reduce noise interference, the CDC was soldered to the back of the board as close to the signal source as possible, as illustrated in **Fig. 1 (a)**. The Silicon Labs EFM32 microcontroller, based on the 32-bit ARM Cortex-M3 core, is used to read the change in sensor capacitance. A Python application with an RS232 serial interface was developed for reading the data.

Data collection was performed by fixing the device to the wrist or finger using a flexible band that gently presses the artery between the sensor and wrist bone, as well as the finger pad. Pressure sensor signals are sampled at 600 Hz. The final data is obtained from the highest quality channel among the three MEMS elements, minimizing signal quality issues due to sensor placement. This is shown in **Fig. 1 (d)**.

B. Human studies

This study used three datasets: Dataset I (D1), Dataset II (D2), and Dataset III (D3). All recordings were performed with subjects remaining supine and silent, using the equipment described in the sensing system section.

D1 consisted of 13 healthy volunteers, including one female, recruited at the University of Turku. D2 included 20 cardiac surgery patients in sinus rhythm (SR), and D3 included 20 patients with persistent AF. In D3, 17 finger recordings (D3F) and 16 wrist recordings (D3W) were collected in total, with some patients contributing both finger and wrist recordings. Gender data was not recorded for D2 and D3. For D1, gender information was available, with one female participant out of 13. This is not expected to affect the study outcomes.

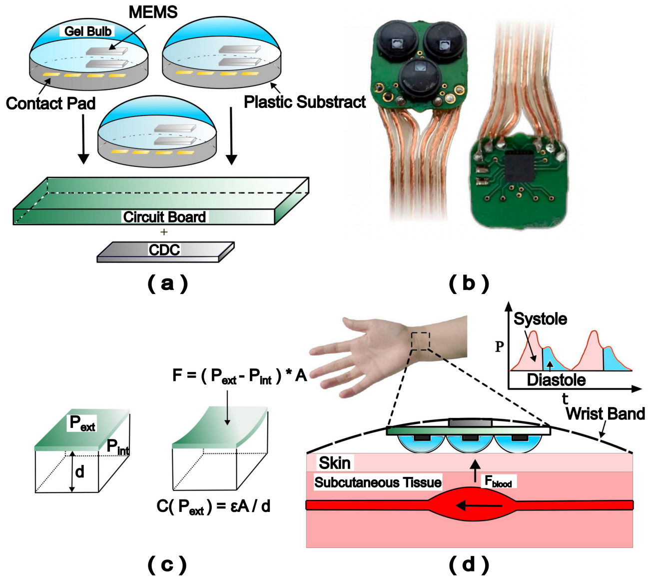

Fig. 1. (a) The circuit board. The three pressure sensor elements are mounted on a printed circuit board. The capacitive-to-digital converter (CDC) is soldered to the back of the board as close to the signal source as possible. (b) The sensor board with sensors. (c) The MEMS principle. One of the silicon wafers forms a diaphragm that bends under external pressure. C = εA/d, where ε is the relative capacitance, A is the area of the diaphragm, and d is the distance between the electrodes. d varies with the bending of the diaphragm. (d) Wrist data acquisition.

Rhythm annotations were assigned based on different references: invasive arterial blood pressure waveforms were used for D2, while D3 relied on clinical diagnoses supported by simultaneous ECG recordings. Measurements for D2 and D3 were conducted at the Heart Center, Turku University Hospital, Finland, with ethical approval from the Ethical Committee of the Hospital District of Southwest Finland and written informed consent from all participants. Measurements for D1 were collected from volunteers at the University of Turku. **Table I** summarizes the baseline characteristics and recording durations for the three datasets.

TABLE I
SUMMARY OF THE DATASETS USED IN THIS STUDY. ALL CONTINUOUS VARIABLES ARE PRESENTED AS MEAN (SD).

Characteristic	D1	D2	D3F	D3W
Rhythm	SR	SR	AF	AF
Number	13	20	17	16
Age (years)	34 (8)	64 (14)	65 (12)	65 (14)
Height (cm)	179 (5)	174 (17)	176 (16)	173 (16)
Weight (kg)	88 (22)	84 (32)	85 (32)	83 (32)
BMI (kg/m^2)	27 (6.0)	28 (10.5)	27.6 (10.3)	27.9 (10.3)
Recording length (min)	1.82 (0.61)	7.41 (3.1)	3.9 (0.82)	3.7 (1.18)

III. ANALYSIS

The signal analysis comprises three distinct stages: A) signal processing, including pre-processing to improve signal quality by removing noise, and peak detection to identify peaks or significant points of interest; B) feature extraction, which extracts relevant features from the signal that can be used for further analysis and classification; C) training and testing machine learning models for classification based on features. The flowchart shown in **Fig. 2** illustrates the different analysis steps used in the study.

A. Signal processing

Firstly, we used a zero-phase fourth-order Butterworth IIR bandpass filter with a frequency range of 0.1 Hz to 25 Hz to remove bias, trend, and high-frequency noise on the signal.

Since pulse waveforms can vary between individuals due to differences in vascular properties, arterial compliance, and peripheral circulation [22] [23] [27], we applied Z-score standardization to normalize the signals and reduce inter-individual variability. Each signal was standardized using the equation $X_{\text{norm}} = \frac{X-\mu}{\sigma}$, where X represents the original signal, μ is the mean, and σ is the standard deviation. This normalization preserves relative variations in signal morphology while making the data more comparable across subjects [22] [28].

Following this, we employed triangular window smoothing, involving convolving the signal with a triangular window function, sized at 15% of the sampling frequency, to further reduce high-frequency noise and suppress the diastolic peak.

Next, the Automatic Multiscale Peak Detection (AMPD) algorithm [29] was applied for peak detection. This algorithm uses a multiscale technique to detect local maxima in the signal, providing robust peak identification despite potential inter-subject variations in pulse waveforms.

At last, the IBI and dIBI were calculated from the detected peak locations. The IBI and dIBI were filtered using a median filter for IBI, which removes outliers and physiological artifacts by rejecting extreme values (e.g., IBI variations of less than 10 ms or greater than 100 ms for dIBI). **Fig. 3** shows the raw and processed signals from SR subjects and AF subjects, as well as the IBI.

B. Feature computation

We use two sets of features: AF-related features for AF detection and morphology-related features for waveform and signal strength analysis. The AF-related features are derived from different signal properties and include an autocorrelation-based feature, autocorrelation area (AUA); an IBI-based feature, Shannon entropy (ShEn); Sample entropy (SampEn); Coefficient of Sample Entropy (CosEn); and three dIBI-based features: mean distance of the points in the Poincaré plot (MDPP), percentage of NN intervals differing over 40 ms (pNN40), and the root mean square of successive differences (RMSSD).The morphology-related features include amplitude, pulse morphology consistency (PMC), and diastolic peak detection ratio (DPDR).

1) AUA: The AUA represents the area between the signal's autocorrelation function and the X-axis [26]. The 30 s segment is obtained after the segmentation, then the 30 s signal is divided into 5 s segments, and the autocorrelation of each segment is calculated and normalized to the range [0, 1]. The absolute value of the average of all segment autocorrelations is then taken. A 4 s overlap is used to calculate the AUA. For AF signals, their amplitude and IBIs are less stable compared to SR signals, and due to their unpredictability, the correlation

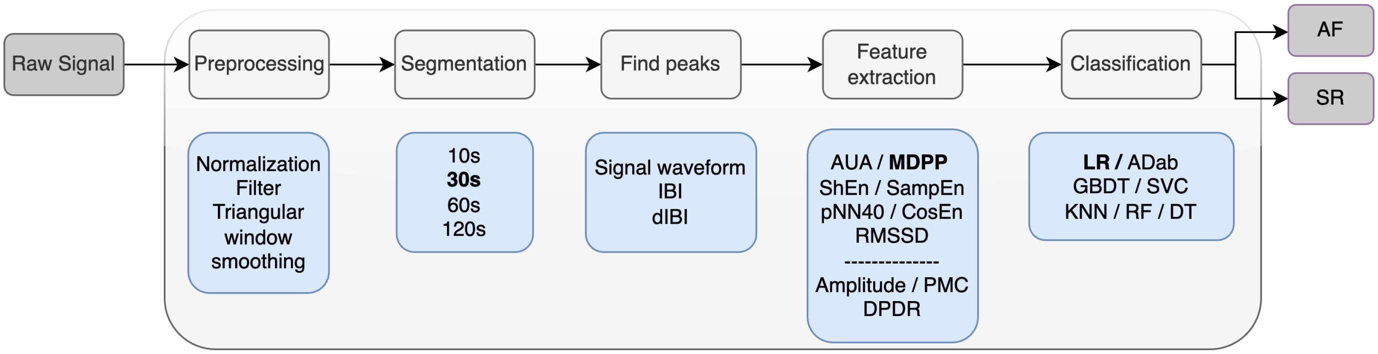

Fig. 2. The AF detection pipeline includes preprocessing, segmentation, peak detection, feature extraction, and classification. Feature extraction covers two sets of features: (1) AF-related features, including Autocorrelation Area (AUA), Mean Distance of Points in the Poincaré Plot (MDPP), Shannon Entropy (ShEn), Sample Entropy (SampEn), proportion of NN intervals greater than 40 ms (pNN40), Cosine Similarity Entropy (CosEn), and Root Mean Square of Successive Differences (RMSSD), used for AF classification; and (2) morphology-related features, including Amplitude, Pulse Morphology Correlation (PMC), and Diastolic Peak to Diastolic Rise (DPDR), used to compare signal strength and waveform differences between finger and wrist. Classification uses seven models: Logistic Regression (LR), AdaBoost (AdaB), Gradient Boosted Decision Tree (GBDT), Support Vector Classification (SVC), K-Nearest Neighbor (KNN), Random Forest (RF), and Decision Tree (DT).

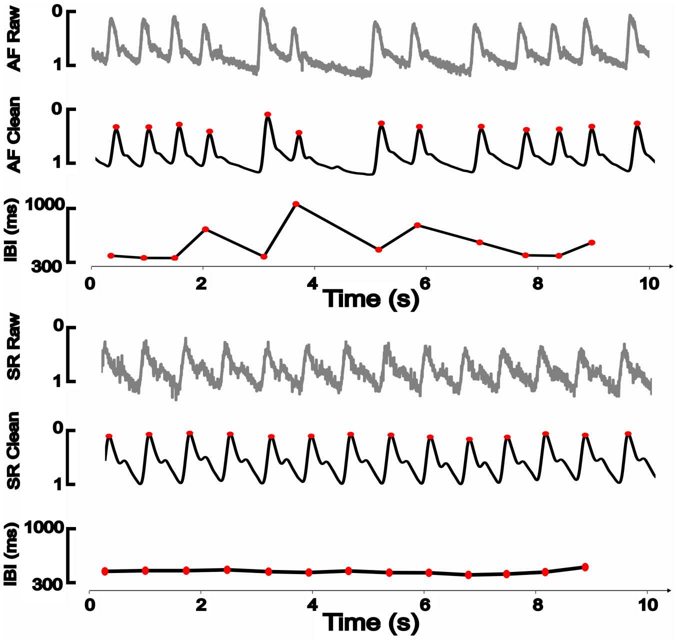

Fig. 3. Typical 10-second **AF** recording before and after pre-processing and 10-second recording of typical **SR** pressure signals before and after pre-processing

of autocorrelation is lower. Hence, we use the autocorrelation function's integral to quantify the autocorrelation change intuitively.

2) MDPP: The MDPP feature is designed for quantifying the complexity and regularity of heartbeat dynamics in physiological signals. This feature is derived from the Poincaré plot, a graphical representation of the relationship between consecutive heartbeat intervals. In the Poincaré plot, each heartbeat is represented by a dot, and the dot's position reflects the relative duration and timing of that beat compared to the previous one. Distances between consecutive points can be obtained from a Poincaré plot consisting of consecutive heartbeat intervals, and then the average of all distances is calculated, which is the result of MDPP. In this case, the distances of consecutive points are obtained by constructing right triangles with the line segment connecting two consecutive points as the hypotenuse, and the lengths of the other two hypotenuses can be expressed as the difference between consecutive heartbeat intervals. Using (1), we calculated the value of the MDPP.

$$MDPP = \frac{1}{n}\sum_{i=1}^{n}\sqrt{(dIBI_{i+1}^2 + dIBI_i^2)} \tag{1}$$

where $dIBI_i = IBI_{i+1} - IBI_i$, we calculated the lengths of the sides of the triangles formed and also the difference between the two successive peak differences.

3) SampEn: SampEn quantifies the complexity or unpredictability in a time series and is widely used to analyze heart rate variability (HRV) and respiratory patterns [30], [31]. It is defined as the negative average natural logarithm of a ratio of counts:

$$SampEn = -\ln\left(\frac{A}{B}\right) \tag{2}$$

where A is the number of patterns of a specified length that occur at least once within a tolerance r, and B is the total number of such patterns in the time series.

4) ShEn: The ShEn quantifies uncertainty or randomness in a dataset [32]. Using (3), we compute ShanEn as follows:

$$ShanEn = -\sum_{i=1}^{n} p_i \log_2 p_i \tag{3}$$

In this formulation, ShanEn denotes the entropy, n the count of possible outcomes, and p_i the probability of the i^{th} outcome.

5) pNN40: The pNN40 is typically used as an indicator of overall heart rate variability and is also thought to reflect parasympathetic activity. It is the proportion of consecutive normal IBIs that differ by more than 40 ms.

6) RMSSD: The RMSSD is a popular measure in heart rate variability analysis. The square root of the mean sum of squares between consecutive IBIs is calculated [33]. Using (4), we calculated the value of RMSSD.

This article has been accepted for publication in IEEE Sensors Journal. This is the author's version which has not been fully edited and content may change prior to final publication. Citation information: DOI 10.1109/JSEN.2025.3574232

$$RMSSD = \sqrt{\frac{1}{n}\sum_{i=1}^{n}(IBI_{i+1} - IBI_i)^2} \tag{4}$$

where n is the number of B-B intervals, and IBI_i is the i^{th} IBI in the pressure sensor signal. The term $(IBI_{i+1} - IBI_i)^2$ represents the square of the difference between successive IBIs.

7) CosEn: CosEn is a modification of SampEn proposed by Lake and Moorman [34], optimized for AF detection by accounting for mean inter-beat intervals (IBIs). Its formula is given by:

$$CosEn = \mathrm{SampEn} + \ln(2r) - \ln\big(\mathrm{mean}(IBI_i)\big) \tag{5}$$

where r is the tolerance parameter, $\mathrm{mean}(IBI_i)$ denotes the average of the IBIs, and SampEn is the negative average natural logarithm of conditional probabilities (see the definition of SampEn).

8) Amplitude: The amplitude feature is the average peak-to-trough difference within pulse segments, calculated as the mean difference between systolic peaks and the lowest points in each segment.

9) PMC: Pulse Morphology Consistency (PMC) measures the similarity of pulse waveforms within a signal. It is calculated by extracting individual waveforms around detected peaks, aligning them to the median waveform, and computing their correlation.

10) DPDR: The Diastolic Peak Detection Ratio (DPDR) is the percentage of diastolic peaks relative to systolic peaks. First, systolic peaks are identified. A search window begins 10% of the IBIs after each systolic peak and ends at the minimum point before the next systolic peak. The first derivative is then applied to locate zero crossings: the first zero crossing indicates the dicrotic notch, and the second, if present, marks the diastolic peak. If only one zero crossing is found, no diastolic peak is recorded. DPDR is computed by dividing the number of detected diastolic peaks by the number of systolic peaks and expressing this value as a percentage.

C. Machine learning classification

To classify subjects as SR and AF, seven machine learning (ML) models were implemented using the scikit-learn library in Python, employing leave-one-subject-out cross-validation. The models were configured as follows: Logistic Regression (LR), set with a maximum iteration limit of 100,000 to ensure convergence; AdaBoost (AdaB) with 100 estimators; Gradient Boosted Decision Tree (GBDT) set with 100 estimators, a learning rate of 1.0, and a maximum depth of 1 to prevent overfitting; K-Nearest Neighbor (KNN) where K was set to 5 based on preliminary testing; Support Vector Classification (SVC) using a linear kernel, 'auto' gamma value, and a degree of 1 to balance complexity and generalization; Random Forest (RF) with 100 estimators and a maximum depth of 5; and a Decision Tree (DT) with a maximum depth of 5.

IV. RESULTS

To evaluate and validate the performance of the proposed features, models, and the overall sensing system, we designed three experiments. (A) Feature-level evaluation consisted of three parts: (A.1) classification performance was evaluated using AF-related features, (A.2) noise robustness was assessed by injecting synthetic noise into the signals and analyzing the resulting performance degradation, and (A.3) morphology-based analysis was performed to compare features extracted from finger and wrist signals. (B) Segment length evaluation examined the effect of different segment lengths, ranging from 10 to 120 seconds, on AF detection performance. (C) Model performance evaluation compared AF detection accuracy across seven machine learning models. Detailed methods and results for each experiment are presented in the following sections and summarized in **Fig. 4**.

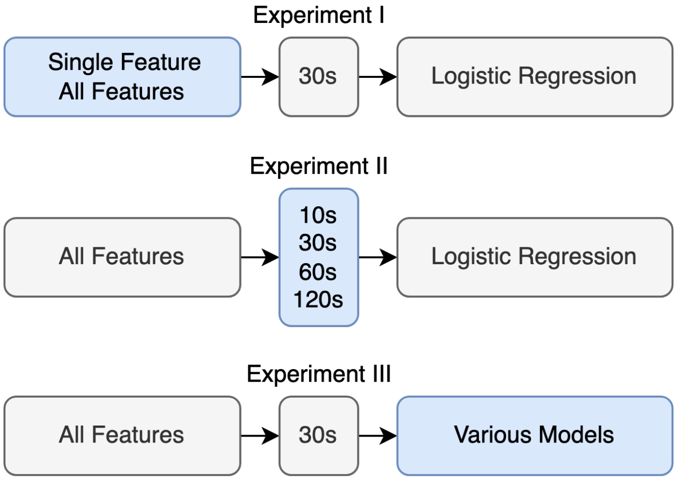

Fig. 4. Flowchart for experiments I, II, and III. All features shown in the figure include AUA, ShEn, SampEn, CosEn, MDPP, pNN40, and RMSSD. Time (s) indicates the segmentation length. The models include LR, AdaB, GBDT, KNN (K=5), SVC, RF, and DT.

A. Experiment I: Feature Evaluation for AF Detection

1) Classification performance of AF-related features: To assess the relative contributions of different features in terms of their impact on the classification of SR and AF, we employed an LR model. Specifically, we examined the performance of individual features when using a fixed segment length of 30 seconds.

Table II presents the performance evaluation of different features in predicting the outcome variable, as assessed by metrics such as Area Under the Receiver Operating Characteristic Curve (AUROC), accuracy, sensitivity, specificity, precision, and F1-score. The results indicate that the performance of the various features varies considerably in their ability to predict the outcome.

Moreover, the model achieves the highest accuracy, sensitivity, and F1-score scores when considering the combined features. The performance comparison based on a single feature shows that the RMSSD consistently achieves high scores across all evaluation metrics, demonstrating notable

TABLE II
PERFORMANCE OF FEATURES

Features	AUROC	Accuracy	Sensitivity	Specificity	Precision	F1
SampEn	0.692	0.625	0.739	0.479	0.644	0.688
ShEn	0.826	0.780	0.776	0.786	0.822	0.798
AUA	0.858	0.784	0.809	0.752	0.806	0.807
CosEn	0.896	0.861	0.832	0.899	0.913	0.870
pNN40	0.910	0.904	0.888	0.924	0.937	0.912
MDPP	0.925	0.913	0.891	0.941	0.951	0.920
RMSSD	0.933	0.919	0.894	0.950	0.958	0.925
All*	0.930	0.919	0.904	0.937	0.948	0.926

This table shows Experiment I results using a 30s segment logistic regression model, where All* represents the combination of seven features.

performance similarity to MDPP. Subsequently, a marginal decrease in classification performance is observed in CosEn, AUA, and ShEn. Conversely, SampEn exhibits the weakest performance. Additionally, the results in **Table II** show that RMSSD achieves similar accuracy as using all features.

2) Robustness to synthetic noise: To systematically evaluate the algorithm's robustness under real-world conditions, we conducted an experiment introducing five types of synthetic noise—realistic walking noise, hand movement noise, muscle artifacts, baseline wander, and model-based 1/f noise with white noise—using the noise generation approach described in [35].

Although the AUROC result of RMSSD in previous experiment is slightly higher than that of using all combined features, the decision to use all features was driven by the need to ensure a robust and generalized algorithm. Our data were collected during short resting-state recordings using three MEMS pressure sensors to capture high-quality signals and minimize artifacts. However, long-term monitoring will inherently introduce noise and artifacts that can compromise signal integrity.

The effects of noise were examined by varying two key parameters: amplitude and duration. The noise amplitudes were scaled relative to the maximum amplitude of the original signal, ranging from 0.0 to 1.0 (0% to 100%) to represent the relative intensity of the noise. In the top plot of **Fig. 5**, each type of noise was added for a fixed duration of 30 s (150 s in total).

The noise duration describes the time that each type of noise was added to the signal. It was varied at 30 s, 60 s, 90 s, and 120 s for each of the five noise types (resulting in total durations of 150 s, 300 s, 450 s, and 600 s, respectively), with the amplitude fixed at 0.3. When the duration exceeded the original signal length, the noise was truncated to match the signal. The results of this test are shown in the bottom plot of **Fig. 5**.

3) Morphology-based analysis and placement comparison: To compare signal characteristics between finger and wrist placements, we computed summary statistics and performed statistical tests, reporting the p-values for all extracted features.

In **Table III**, wrist signals generally have higher amplitude than finger signals, indicating stronger waveforms that facilitate feature detection. However, in DS2 (post-cardiac surgery group), wrist amplitude is lower than finger signals, likely due to hemodynamic differences. In terms of PMC, DS1 (healthy volunteers) shows the highest signal consistency in wrist (0.8 ± 0.2), while AF finger signals show the lowest (0.5 ± 0.2), possibly due to lower signal quality and AF-related irregularities affecting peak detection and IBI stability. Additionally, in only 46.8% of finger signals a diastolic peak is detected compared to 93.6% in healthy wrist signals, as indicated by the DPDR, further suggesting weaker finger waveforms. These differences align with prior findings that wrist-based signals tend to exhibit higher amplitude and more distinct systolic and diastolic peaks than finger-based signals, which are more damped due to higher vascular resistance and greater distance from central circulation [36], [37].

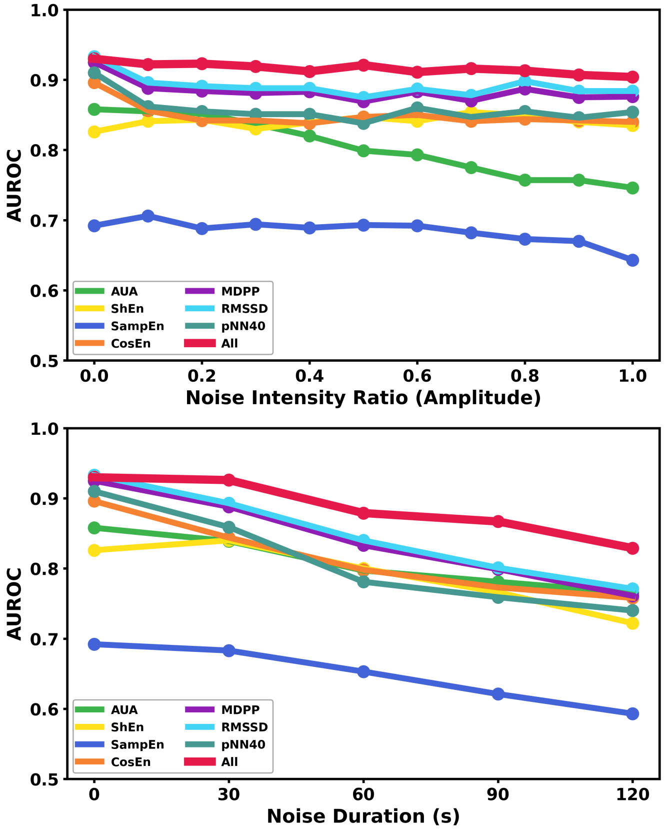

Fig. 5. The top plot shows AUROC as a function of relative noise intensity, defined as the ratio of noise amplitude to the maximum signal amplitude, ranging from 0.0 to 1.0. The duration of added noise is fixed at 30 s (150 s in total). The bottom plot shows AUROC as a function of the duration of added noise, tested at 30 s, 60 s, 90 s, and 120 s for each type of noise (150 s, 300 s, 450 s, and 600 s in total for the five noise types). The relative noise intensity ratio is fixed at 0.3.

Despite these waveform differences, key AF detection features remain structurally similar between wrist and finger signals, indicating that variations in signal strength do not significantly impact AF detection performance. Additionally, **Table III** shows that D1-D3W and D2-D3W exhibit significant differences in all features ($P < 0.001$), demonstrating a strong distinction between SR and AF signals. Although D1-D2 shows significant differences in ShEn, CosEn, MDPP and RMSSD, these differences do not affect AF. This suggests that despite variations between young (D1) and post-cardiac surgery (D2) SR groups, their impact on AF detection remains minimal. Hence, our method effectively shows AF detection

TABLE III

BOXPLOT STATISTICS FOR ALL FEATURES (MEAN ± STD) AND P-VALUES (T-TEST) ACROSS DIFFERENT DATASETS. D1: DS1 (HEALTHY VOLUNTEERS SR, WRIST), D2: DS2 (POSTOPERATIVE SR, WRIST), D3F: DS3 (AF, FINGER), D3W: DS3 (AF, WRIST).

Category	**Feature**	**Mean ± STD**				**P-values**			
		D1	**D2**	**D3F**	**D3W**	**D1-D2**	**D3W-D3F**	**D1-D3W**	**D2-D3W**
AF-related	AUA	1.6 ± 0.3	1.6 ± 0.2	1.2 ± 0.2	1.2 ± 0.2	0.423	0.007	< 0.001	< 0.001
	SampEn	1.1 ± 0.5	0.9 ± 0.6	1.3 ± 0.4	1.4 ± 0.6	0.031	0.081	0.016	< 0.001
	ShEn	2.8 ± 0.2	2.4 ± 0.5	3.1 ± 0.3	3.1 ± 0.3	< 0.001	0.560	< 0.001	< 0.001
	CosEn	-2.7 ± 0.6	-3.6 ± 1.1	-1.6 ± 0.6	-1.6 ± 0.8	< 0.001	0.965	< 0.001	< 0.001
	MDPP	31.1 ± 17.9	17.8 ± 19.9	66.2 ± 14.1	67.3 ± 13.9	< 0.001	0.852	< 0.001	< 0.001
	RMSSD	25.1 ± 13.4	15.1 ± 14.7	51.2 ± 9.3	51.8 ± 8.7	< 0.001	0.899	< 0.001	< 0.001
	pNN40	16.2 ± 15.6	13.6 ± 22.7	66.2 ± 13.8	65.2 ± 15.0	0.351	0.408	< 0.001	< 0.001
Morphology-related	Amplitude	2.8 ± 0.9	1.0 ± 0.9	1.2 ± 0.7	1.7 ± 1.0	< 0.001	< 0.001	< 0.001	0.008
	PMC	0.8 ± 0.2	0.6 ± 0.2	0.5 ± 0.2	0.7 ± 0.1	< 0.001	< 0.001	< 0.001	< 0.001
	DPDR	93.6 ± 6.4	83.6 ± 18.5	46.8 ± 36.0	89.0 ± 15.3	< 0.001	< 0.001	< 0.001	< 0.001

TABLE IV

PERFORMANCE OF LENGTHS

Length	AUROC	Accuracy	Sensitivity	Specificity	Precision	F1
10s	0.927	0.894	0.894	0.895	0.915	0.904
30s	0.930	0.919	0.904	0.937	0.948	0.926
60s	0.940	0.917	0.902	0.937	0.949	0.925
120s	0.935	0.911	0.904	0.920	0.943	0.923

Table presents the outcomes of Experiment II, utilizing logistic regression models with All* features and varying signal lengths.

TABLE V

PERFORMANCE OF MODELS

Models	AUROC	Accuracy	Sensitivity	Specificity	Precision	F1
LR	0.930	0.919	0.904	0.937	0.948	0.926
ADab	0.911	0.880	0.871	0.891	0.910	0.890
GBDT	0.913	0.896	0.878	0.920	0.933	0.905
SVC	0.926	0.913	0.894	0.937	0.948	0.920
KNN	0.920	0.896	0.881	0.916	0.930	0.905
RF	0.934	0.922	0.911	0.937	0.948	0.929
DT	0.910	0.895	0.888	0.903	0.921	0.904

Table displays the results of Experiment III, featuring 30s segments and All* features, across various machine learning models.

robustness in peripheral pressure signals.

B. Experiment II: Evaluation of different lengths of signal

To compare the effect of different signal segment lengths on the classification results, in Experiment II, a logistic regression model was used to test the performance of the combination of all features at different segment lengths (10 s, 30 s, 60 s, and 120 s).

The model performed well overall, with AUROC ranging from 0.927 to 0.940. The highest AUROC was achieved on the 60 s dataset, and according to **Table IV**, The accuracy ranged from 0.894 to 0.919, achieving the highest accuracy on the 30 s data set. On the other hand, the specificity ranged from 0.895 to 0.937, indicating the model's ability to identify negative samples correctly. The precision of the model ranged from 0.915 to 0.949, indicating the proportion of true positive predictions among all positive predictions. The F1-score ranged from 0.904 to 0.926. The results suggest that their performance is not significantly affected by changes in segment length. Based on these findings and clinical recommendations, we chose the commonly used 30 s segment length for subsequent experiments and comparisons.

C. Experiment III: Model Performance Evaluation

To verify the performance of our features on all models, in Experiment III, in addition to LR models, we tested the performance of six other popular machine learning algorithms: ADab, GBDT, SVC, KNN, RF, and DT. Each signal was segmented into 30 s windows, and the feature set included all available features. Our model exhibited stable performance across varying random seeds.

Table V presents the performance metrics, including AUROC, accuracy, sensitivity, specificity, precision, and F1-score, for various ML models.

Among the evaluated models, the RF consistently achieved the highest values across all performance metrics. LR also yielded nearly identical results to RF. The AUROC values for these seven models ranged from 0.910 to 0.934. Additionally, the specificity and precision of the SVC model were consistent with LR and RF, with values of 0.937 and 0.948, respectively. These findings indicate that our features performed well across all machine learning models, demonstrating the effectiveness of the proposed algorithm in classification tasks.

V. DISCUSSION

In this study, we conducted a comprehensive evaluation of a pressure sensor system based on MEMS, aimed at detecting AF. Our validation process primarily examined the accuracy of data acquisition by the sensor components at both wrist and finger locations. The sensor not only captures data with high precision but also demonstrates advantages in low power consumption and cost-effectiveness, enabling potential for long-term monitoring without frequent recharging. This makes it particularly suited for detecting intermittent AF events through continuous monitoring. Notably, in the third dataset, we implemented a multi-point monitoring approach, collecting signals from the wrists and fingers of AF patients in a hospital setting. This non-invasive monitoring method in a hospital setting represents a novel attempt in the field.

This article has been accepted for publication in IEEE Sensors Journal. This is the author's version which has not been fully edited and content may change prior to final publication. Citation information: DOI 10.1109/JSEN.2025.3574232

Furthermore, we introduced a new feature called MDPP, which showed exceptional performance in AF classification.

The AUA feature is a non-peak detection feature that does not require peak detection. In the case of patients with AF, their signals lack the pseudo-periodic pattern that is usually present in SR recordings. As a result, the area formed by the autocorrelation function becomes small. This property makes AUA a valid choice when peaks are difficult to detect.

The dIBI-based features MDPP, pNN40, and RMSSD have consistently shown superior performance in our dataset and other studies conducted in the field. In a study by Corino *et al.* [38], a wristband device was used to detect AF, demonstrating that pNN40 and pNN70 achieved an AF classification accuracy of 91.0%. In addition, Eerikäinen *et al.* [39] developed a classifier using pNN70, ShEn, and SampEn to detect AF, achieving a sensitivity of 97.2% and a specificity of 98.2%. Several studies have investigated the effectiveness of RMSSD in detecting AF using different devices and settings. Chang *et al.* [40] reported a sensitivity of 97.3% for AF detection using smartwatch PPG recordings.

Regarding MDPP, it has demonstrated comparable performance to pNN40 and RMSSD. MDPP is a new feature extracted from a Poincaré plot. The plot maps a one-dimensional signal onto a two-dimensional space and is a visual representation of the dynamic characteristics of a signal. It is a nonlinear method for revealing hidden correlation patterns in a time series signal. The points in the plot outline a trajectory that describes the system's evolution and is commonly used to assess the dynamics of heart rate variability [41]. Based on the results of the Poincaré plots, we observed that the MDPP values were smaller in the healthy group than in the AF group.

In the Poincaré plot, the 45 degree diagonal line represents the situation when $IBI_{i+1} = IBI_i$, indicating that the two successive peak intervals are the same. However, for patients with AF, their heartbeats are irregular and chaotic and there is a large span between the points on their Poincaré plots.

Some IBI entropy-based features were also applied in this study. In the paper by Tang *et al.* [42], the authors identified six features from the 2-minute segment achieving an AUC of 0.972 for AF detection. In the paper by Bashar *et al.* (2019) [43], they combined RMSSD, SampEn, and a weighted feature of the two to detect AF, achieving 94.3% accuracy. Shan *et al.* (2016) [44] used 12 features in total, with a cost-sensitive SVM, achieving an AUC of 0.971 for AF detection from PPG signals.

At the same time, combining all of the features produces the most effective results. Combining different types of features can maximize the extraction of information from the original signal, thereby obtaining the best results. This demonstrates the importance of feature selection and integration in signal processing and analysis. Our experimental results show that the AUROCs obtained for signals of different segment lengths are in the order of greater than 60 s over 120 s over 30 s over 10 s, but the difference between the AUROC obtained for the 60 s segment and the 120 s segment is only 0.005, and there is almost no difference between the results obtained for the four segment lengths.

The study faces three primary limitations. First, strap tightness, sensor location and hand movements influence the quality of signal collection. Second, the dataset's complexity, reflected in its diversity of collection groups and locations, spans healthy young individuals, elderly post-cardiac surgery patients, and older individuals with AF undergoing hospital interventions, with data from both wrists and fingers. Despite this, our classification system demonstrates robust generalization capabilities with strong results. Third, while the noise-added experiments simulate various realistic artifacts from long-term monitoring, they do not fully reflect real-world conditions. Future research will focus on collecting long-duration data and personalizing models through online learning or incremental updates to improve AF detection accuracy in practical applications.

VI. CONCLUSION

This study validated a MEMS-based wearable pressure sensor system designed for continuous AF monitoring. Data were collected from 53 participants, with measurements obtained from both the wrist and finger. The system achieved high classification accuracy, supported by a carefully designed feature set capturing beat-to-beat irregularities. While motion artifacts and real-world noise can degrade signal quality, synthetic noise injection experiments demonstrated that the proposed algorithm maintained robust performance across varying amount of noise. The results further show the influence of sensor placement, segment length, feature selection, and noise robustness, providing a comprehensive evaluation of this MEMS-based sensing system's.

REFERENCES

[1] S. S. Chugh, R. Havmoeller, K. Narayanan, D. Singh, M. Rienstra, E. J. Benjamin, R. F. Gillum, Y.-H. Kim, J. H. McAnulty Jr, Z.-J. Zheng *et al.*, "Worldwide epidemiology of atrial fibrillation: a global burden of disease 2010 study," *Circulation*, vol. 129, no. 8, pp. 837–847, 2014.

[2] E. Benjamin, M. Blaha, S. Chiuve, M. Cushman, S. Das, R. Deo *et al.*, "Comité de estadísticas y del subcomité de estadísticas de ataque cerebral de la american heart association. estadísticas de enfermedad cardíaca y de ataque cerebral. información actualizada para 2017: Informe de american heart association," *Circulation*, vol. 135, pp. e146–603, 2017.

[3] J. Jaakkola, S. Jaakkola, O. Lahdenoja, T. Hurnanen, T. Koivisto, M. Pänkäälä, T. Knuutila, T. O. Kiviniemi, T. Vasankari, and K. J. Airaksinen, "Mobile phone detection of atrial fibrillation with mechanocardiography: the mode-af study (mobile phone detection of atrial fibrillation)," *Circulation*, vol. 137, no. 14, pp. 1524–1527, 2018.

[4] G. H. Tison, J. M. Sanchez, B. Ballinger, A. Singh, J. E. Olgin, M. J. Pletcher, E. Vittinghoff, E. S. Lee, S. M. Fan, R. A. Gladstone *et al.*, "Passive detection of atrial fibrillation using a commercially available smartwatch," *JAMA cardiology*, vol. 3, no. 5, pp. 409–416, 2018.

[5] Y. Guo, H. Wang, H. Zhang, T. Liu, Z. Liang, Y. Xia, L. Yan, Y. Xing, H. Shi, S. Li *et al.*, "Mobile health technology for atrial fibrillation screening using photoplethysmography-based smart devices: The huawei heart study," *J. Am. Coll. Cardiol*, vol. 74, no. 19, pp. 2365–2375, 2019.

[6] M. P. Turakhia, S. A. Desai, and R. A. Harrington, "The outlook of digital health for cardiovascular medicine: challenges but also extraordinary opportunities," *JAMA cardiology*, vol. 1, no. 7, pp. 743–744, 2016.

[7] P. Francia, C. Adduci, L. Semprini, F. Palano, D. Santini, B. Musumeci, C. Santolamazza, M. Volpe, and C. Autore, "Prognostic implications of defibrillation threshold testing in patients with hypertrophic cardiomyopathy," *Journal of Cardiovascular Electrophysiology*, vol. 28, no. 1, pp. 103–108, 2017.

[8] Y. Zou, A. Libanori, J. Xu, A. Nashalian, and J. Chen, "Triboelectric nanogenerator enabled smart shoes for wearable electricity generation," *Research*, 2020.

[9] C.-L. Choong, M.-B. Shim, B.-S. Lee, S. Jeon, D.-S. Ko, T.-H. Kang, J. Bae, S. H. Lee, K.-E. Byun, J. Im *et al.*, "Highly stretchable resistive pressure sensors using a conductive elastomeric composite on a micropyramid array," *Advanced materials*, vol. 26, no. 21, pp. 3451–3458, 2014.

[10] J. C. Yang, J.-O. Kim, J. Oh, S. Y. Kwon, J. Y. Sim, D. W. Kim, H. B. Choi, and S. Park, "Microstructured porous pyramid-based ultrahigh sensitive pressure sensor insensitive to strain and temperature," *ACS applied materials & interfaces*, vol. 11, no. 21, pp. 19 472–19 480, 2019.

[11] G. Schwartz, B. C.-K. Tee, J. Mei, A. L. Appleton, D. H. Kim, H. Wang, and Z. Bao, "Flexible polymer transistors with high pressure sensitivity for application in electronic skin and health monitoring," *Nature communications*, vol. 4, no. 1, p. 1859, 2013.

[12] D. L. Presti, C. Massaroni, D. Formica, P. Saccomandi, F. Giurazza, M. A. Caponero, and E. Schena, "Smart textile based on 12 fiber bragg gratings array for vital signs monitoring," *IEEE Sensors Journal*, vol. 17, no. 18, pp. 6037–6043, 2017.

[13] X. Yang, Z. Chen, C. S. M. Elvin, L. H. Y. Janice, S. H. Ng, J. T. Teo, and R. Wu, "Textile fiber optic microbend sensor used for heartbeat and respiration monitoring," *IEEE Sensors Journal*, vol. 15, no. 2, pp. 757–761, 2014.

[14] C. Dagdeviren, Y. Su, P. Joe, R. Yona, Y. Liu, Y.-S. Kim, Y. Huang, A. R. Damadoran, J. Xia, L. W. Martin *et al.*, "Conformable amplified lead zirconate titanate sensors with enhanced piezoelectric response for cutaneous pressure monitoring," *Nature communications*, vol. 5, no. 1, p. 4496, 2014.

[15] Y. Xi, S. Cheng, S. Chao, Y. Hu, M. Cai, Y. Zou, Z. Liu, W. Hua, P. Tan, Y. Fan *et al.*, "Piezoelectric wearable atrial fibrillation prediction wristband enabled by machine learning and hydrogel affinity," *Nano Research*, pp. 1–8, 2023.

[16] H. Ouyang, J. Tian, G. Sun, Y. Zou, Z. Liu, H. Li, L. Zhao, B. Shi, Y. Fan, Y. Fan *et al.*, "Self-powered pulse sensor for antidiastole of cardiovascular disease," *Advanced Materials*, vol. 29, no. 40, p. 1703456, 2017.

[17] X. Wang, J. Yang, K. Meng, Q. He, G. Zhang, Z. Zhou, X. Tan, Z. Feng, C. Sun, J. Yang *et al.*, "Enabling the unconstrained epidermal pulse wave monitoring via finger-touching," *Advanced Functional Materials*, vol. 31, no. 32, p. 2102378, 2021.

[18] Y. Zhou, X. Zhao, J. Xu, Y. Fang, G. Chen, Y. Song, S. Li, and J. Chen, "Giant magnetoelastic effect in soft systems for bioelectronics," *Nature Materials*, vol. 20, no. 12, pp. 1670–1676, 2021.

[19] E. Mejia-Mejia, J. Allen, K. Budidha, C. El-Hajj, P. A. Kyriacou, and P. H. Charlton, "Photoplethysmography signal processing and synthesis," in *Photoplethysmography*. Elsevier, 2022, pp. 69–146.

[20] C. El-Hajj and P. A. Kyriacou, "A review of machine learning techniques in photoplethysmography for the non-invasive cuff-less measurement of blood pressure," *Biomedical Signal Processing and Control*, vol. 58, p. 101870, 2020.

[21] J. Allen and A. Murray, "Age-related changes in the characteristics of the photoplethysmographic pulse shape at various body sites," *Physiological measurement*, vol. 24, no. 2, p. 297, 2003.

[22] J. Allen, "Photoplethysmography and its application in clinical physiological measurement," *Physiological measurement*, vol. 28, no. 3, p. R1, 2007.

[23] M. Elgendi, "On the analysis of fingertip photoplethysmogram signals," *Current cardiology reviews*, vol. 8, no. 1, pp. 14–25, 2012.

[24] M. S. Khan, M. O. Tariq, M. Nawaz, and J. Ahmed, "Mems sensors for diagnostics and treatment in the fight against covid-19 and other pandemics," *IEEE Access*, vol. 9, pp. 61 123–61 149, 2021.

[25] M. Kaisti, J. Leppänen, O. Lahdenoja, P. Kostiainen, M. Pankaaia, U. Meriheina, and T. Koivisto, "Wearable pressure sensor array for health monitoring," in *2017 Computing in Cardiology (CinC)*. IEEE, 2017, pp. 1–4.

[26] M. Kaisti, T. Panula, J. Leppänen, R. Punkkinen, M. Jafari Tadi, T. Vasankari, S. Jaakkola, T. Kiviniemi, J. Airaksinen, P. Kostiainen *et al.*, "Clinical assessment of a non-invasive wearable mems pressure sensor array for monitoring of arterial pulse waveform, heart rate and detection of atrial fibrillation," *NPJ digital medicine*, vol. 2, no. 1, p. 39, 2019.

[27] P. H. Charlton, B. Paliakaitė, K. Pilt, M. Bachler, S. Zanelli, D. Kulin, J. Allen, M. Hallab, E. Bianchini, C. C. Mayer *et al.*, "Assessing hemodynamics from the photoplethysmogram to gain insights into vascular age: a review from vascagenet," *American Journal of Physiology-Heart and Circulatory Physiology*, vol. 322, no. 4, pp. H493–H522, 2022.

[28] J. Allen, J. O'Sullivan, G. Stansby, and A. Murray, "Age-related changes in pulse risetime measured by multi-site photoplethysmography," *Physiological Measurement*, vol. 41, no. 7, p. 074001, 2020.

[29] F. Scholkmann, J. Boss, and M. Wolf, "An efficient algorithm for automatic peak detection in noisy periodic and quasi-periodic signals," *Algorithms*, vol. 5, no. 4, pp. 588–603, 2012.

[30] D. E. Lake, J. S. Richman, M. P. Griffin, and J. R. Moorman, "Sample entropy analysis of neonatal heart rate variability," *American Journal of Physiology-Regulatory, Integrative and Comparative Physiology*, 2002.

[31] J. S. Richman and J. R. Moorman, "Physiological time-series analysis using approximate entropy and sample entropy," *American journal of physiology-heart and circulatory physiology*, 2000.

[32] C. E. Shannon, "A mathematical theory of communication," *The Bell system technical journal*, vol. 27, no. 3, pp. 379–423, 1948.

[33] H. V. Huikuri, T. Mäkikallio, K. J. Airaksinen, R. Mitrani, A. Castellanos, and R. J. Myerburg, "Measurement of heart rate variability: a clinical tool or a research toy?" *Journal of the American College of Cardiology*, vol. 34, no. 7, pp. 1878–1883, 1999.

[34] D. E. Lake and J. R. Moorman, "Accurate estimation of entropy in very short physiological time series: the problem of atrial fibrillation detection in implanted ventricular devices," *American Journal of Physiology-Heart and Circulatory Physiology*, vol. 300, no. 1, pp. H319–H325, 2011.

[35] K. Karhinoja, A. Vasankari, J.-P. Sirkiä, A. Airola, D. Wong, and M. Kaisti, "Flexible framework for generating synthetic electrocardiograms and photoplethysmograms," *arXiv preprint arXiv:2408.16291*, 2024.

[36] E. Mejía-Mejía, K. Budidha, T. Y. Abay, J. M. May, and P. A. Kyriacou, "Heart rate variability (hrv) and pulse rate variability (prv) for the assessment of autonomic responses," *Frontiers in physiology*, vol. 11, p. 779, 2020.

[37] A. Saglietto, S. Scarsoglio, D. Canova, G. M. De Ferrari, L. Ridolfi, and M. Anselmino, "Beat-to-beat finger photoplethysmography in atrial fibrillation patients undergoing electrical cardioversion," *Scientific Reports*, vol. 13, no. 1, p. 6751, 2023.

[38] V. D. Corino, R. Laureanti, L. Ferranti, G. Scarpini, F. Lombardi, and L. T. Mainardi, "Detection of atrial fibrillation episodes using a wristband device," *Physiological measurement*, vol. 38, no. 5, p. 787, 2017.

[39] L. M. Eerikäinen, A. G. Bonomi, F. Schipper, L. R. Dekker, H. M. de Morree, R. Vullings, and R. M. Aarts, "Detecting atrial fibrillation and atrial flutter in daily life using photoplethysmography data," *IEEE journal of biomedical and health informatics*, vol. 24, no. 6, pp. 1610–1618, 2019.

[40] P.-C. Chang, M.-S. Wen, C.-C. Chou, C.-C. Wang, and K.-C. Hung, "Atrial fibrillation detection using ambulatory smartwatch photoplethysmography and validation with simultaneous holter recording," *American Heart Journal*, vol. 247, pp. 55–62, 2022.

[41] R. A. Hoshi, C. M. Pastre, L. C. M. Vanderlei, and M. F. Godoy, "Poincaré plot indexes of heart rate variability: relationships with other nonlinear variables," *Autonomic Neuroscience*, vol. 177, no. 2, pp. 271–274, 2013.

[42] S.-C. Tang, P.-W. Huang, C.-S. Hung, S.-M. Shan, Y.-H. Lin, J.-S. Shieh, D.-M. Lai, A.-Y. Wu, and J.-S. Jeng, "Identification of atrial fibrillation by quantitative analyses of fingertip photoplethysmogram," *Scientific reports*, vol. 7, no. 1, pp. 1–7, 2017.

[43] S. K. Bashar, D. Han, S. Hajeb-Mohammadalipour, E. Ding, C. Whitcomb, D. D. McManus, and K. H. Chon, "Atrial fibrillation detection from wrist photoplethysmography signals using smartwatches," *Scientific reports*, vol. 9, no. 1, pp. 1–10, 2019.

[44] S.-M. Shan, S.-C. Tang, P.-W. Huang, Y.-M. Lin, W.-H. Huang, D.-M. Lai, and A.-Y. A. Wu, "Reliable ppg-based algorithm in atrial fibrillation detection," in *2016 IEEE Biomedical Circuits and Systems Conference (BioCAS)*. IEEE, 2016, pp. 340–343.